Synthesis of Amino Acids by Electrocatalytic Reduction of CO2 on Chiral Cu Surfaces

Yuxi Fang

Tongji University

Xi Liu

Shanghai Jiao Tong University   https://orcid.org/0000-0002-8654-0774

Zhipan Liu

Fudan University   https://orcid.org/0000-0002-2906-5217

Lu Han

Tongji University   https://orcid.org/0000-0002-6119-4895

Jing Ai

Tongji University

Gui Zhao

Shanghai Jiao Tong University

Osamu Terasaki

ShanghaiTech Universtiy   https://orcid.org/0000-0001-5803-0817

Cunhao Cui

Shanghai Jiao Tong University

Jiuzhong Yang

University of Science and Technology of China

Chengyuan Liu

University of Science and Technology of China

Zhongyue Zhou

Shanghai Jiao Tong University   https://orcid.org/0000-0002-5576-1400

Liwei Chen

Shanghai Jiao Tong University

Shunai Che (✉ chesa@sjtu.edu.cn)

Shanghai Jiao Tong University

Article

Keywords:

DOI: https://doi.org/10.21203/rs.3.rs-1479745/v1

Synthesis of Amino Acids by Electrocatalytic Reduction of CO₂ on Chiral Cu Surfaces

Yuxi Fang[1†], Xi Liu[2,4†], Zhipan Liu[3*], Lu Han[1*], Jing Ai[1], Gui Zhao[4], Osamu Terasaki[5], Cunhao Cui[6], Jiuzhong Yang[7†], Chengyuan Liu[7], Zhongyue Zhou[6*], Liwei Chen[2,4] & Shunai Che[1,2*]

[1]School of Chemical Science and Engineering, Tongji University, 1239 Siping Road, Shanghai, 200092, China. [2]School of Chemistry and Chemical Engineering, Frontiers Science Center for Transformative Molecules, State Key Laboratory of Metal Matrix Composites, Shanghai Key Laboratory for Molecular Engineering of Chiral Drugs, Shanghai Jiao Tong University, 800 Dongchuan Road, Shanghai, 200240, China. [3]Collaborative Innovation Centre of Chemistry for Energy Material, Shanghai Key Laboratory of Molecular Catalysis and Innovative Materials, Key Laboratory of Computational Physical Science, Department of Chemistry, Fudan University, 2005 Songhu Road, Shanghai, 200438, China. [4]School of Chemical Science and Engineering, In-situ Centre for Physical Science, Shanghai Jiao Tong University, 800 Dongchuan Road, Shanghai, 200240, China. [5]Centre for High resolution Electron Microscopy & Shanghai Key Lab of High-resolution Microscopy, ShanghaiTech University, Shanghai, 201210, China. [6]School of Mechanical Engineering, Shanghai Jiao Tong University, 800 Dongchuan Road, Shanghai, 200240, China. [7]National Synchrotron Radiation Laboratory, University of Science and Technology of China, 42 Hezuohua South Road, Hefei, Anhui, 230029, China.

† These authors contributed equally to this work. *e-mail: chesa@sjtu.edu.cn; zpliu@fudan.edu.cn; luhan@tongji.edu.cn; zhongyue.zhou@sjtu.edu.cn

CO₂ reduction and fixation products ranging from small molecules to biomolecules, are highly diverse in natural systems. Athough various multicarbon products of CO₂ reduction were artificially obtained, the C₃₊ products with various functional groups (e.g., C-N and C=O bonds), especially biomolecules, have never been reported. Herein, we synthesized C₃₊ amino acids *via* electrocatalytic reduction from CO₂ and NH₃ using chiral Cu films (CCFs) as electrodes. Electron microscopy and theoretical calculations suggested that chiral kink sites Cu(653) is the most likely formed on the surface of CCFs fabricated by electrodeposition in the presence of Histidine (His). Serine (Ser), with an enantiomeric excess (*ee*) greater than 90% is the main component of various amino acids. Experimental and computational data showed that the 3-hydropyruvic acid formation from H₂CO⁻CO* is the stereo-determining step in the Ser formation pathway. The Cu(653) was speculated to be restricting the configuration changes of C₃₊ intermediates to involve a thermodynamically and kinetically favourable formation of enantiomeric Ser.

Cu and Cu alloys are known to be the main family of catalysts for the electroreduction of CO₂ to multicarbon products, C_1-C_2 molecules and C_{3-4} aliphatic alcohols[1-14]. Nevertheless, the CO₂ reduction products with C-N bonds are limited in only C_1-C_2 species (urea, methylamine, ethylamine and acetamide)[13-16]. It has been reported experimentally and theoretically that the configuration of atoms on catalysts surfaces could increase intrinsic catalytic activity of Cu based catalysts for CO₂ reduction *via* decrease energy barrier in reaction pathways[17-19]. However, enhancement of previously reported active sites on Cu surfaces was only observed in C_{1-2} molecules and n-propanol[3,4,17-19].

Herein, our approach is to create chiral kink sites with high Miller index on Cu surfaces to activate unconventional C_{3+} production pathway of electrocatalytic reduction of CO₂ to amino acids (Fig. S1). The energy barrier of the reactions would be decreased by electrostatic interaction and coordination effect due to geometrically arranged low-coordinated metal species in chiral kink sites[20-22]. Meanwhile, enantioselectivity of amino acids would be achieved by chiral atomic surfaces due to different affinity of amino acids enantiomers with difference geometric configuration[23-26]. Herein, the chiral kink sites were generated on the surface of chiral molecule-induced CCFs along with electroreduction of Cu ions interacted with chiral molecules dissolved in electrolyte on conductive substrate.

Fabrication of CCFs

CCFs were electrodeposited from $[CuCl_4]^{2-}$ with the assistance of chiral molecules and the removal of organic components to generate Cu chiral surfaces at the atomic level (see Method section for details). Ni foil was selected as both the working electrode and the substrate. The electrolyte was composed of hexadecyltrimethyl ammonium chloride (CTAC), His, nickel chloride, potassium tetrachlorocuprate, potassium chloride, hydrochloric acid and deionized water. L/D-His was chosen as both the structure-directing agent and the symmetry-breaking agent for asymmetric attachment and cooperative self-assembly with Cu ions because of the coordinating interaction between these species to form chiral kink sites. Potassium chloride was added to the solution to prevent $[CuCl_4]^{2-}$ decomposition; Ni^{2+} ions in solution could facilitate the formation of Cu dendrite[27]. Due to the steric hindrance of CTAC, Cu nanoparticles were electrodeposited uniformly on the Ni foil by the reduction of Cu ions. The organics in the as-synthesized

CCFs (CCFs-as) could be completely removed after electrochemical cleaning (Fig. S2) to obtain final pure inorganic product CCFs without organics. The final products synthesized with L- and D-His were defined as L- and D-CCFs, respectively. For comparison, the achiral Cu films (ACFs) were prepared without any chiral molecules. The same Cu states, the absence of both organics and Ni on the surface of the CCFs and ACFs were confirmed by X-ray photoelectron spectroscopy (XPS) (Fig. S3).

Characterization of CCFs

Fig. 1a shows the wide-angle X-ray diffraction (XRD) patterns of L-CCFs and ACFs. The reflections can be indexed as 111, 200, 220 and 311 (corresponding to blue standard bars) according to the face-centred cubic (FCC) phase of Cu with a space group of $Fm\overline{3}m$ and lattice parameters of $a = 3.608 \pm 0.005$ Å for JCPDS no. 01-1241 for all samples. The other intense neighbouring reflections are associated with the Ni substrate (corresponding to green standard bars). No additional peaks for other crystalline byproducts were observed. Considering the lattice parameter of Ni ($a = 3.529$ Å for JCPDS no. 04-0850, space group of $Fm\overline{3}m$) is obvious different, all samples herein should be pure Cu without the formation of Ni alloys. Notably, the reflection intensities of the ACFs are the same as those of the bulk sample (JCPDS no. 01-1241), while the relative intensity of the 200 reflections in the L- and D-CCFs is significantly higher than that of the ACFs (Fig S4). In addition, the relative intensities of the 111 and 220 reflections in the CCFs are much lower. These results suggest the possible preferred orientation or the repeating units along <100>.

Scanning electron microscopy (SEM) images of L-CCFs (Fig. 1b₁ and b₂) show that the films are composed of a flat arrangement of fusiform Cu nanoparticles with uniform in size (~50 nm in diameter and ~200 nm in length). The light contrast in the high-magnification SEM image reveals the unsmooth surface with small buds grown on the Cu surface, which is confirmed by transmission electron microscopy (TEM) investigations. The same morphologies were observed in the SEM images of D-CCFs (Fig. S4a₂ and a₃). The SEM images of ACFs (Fig. S4b₂ and b₃) show that the films are composed of polyhedral Cu nanocrystals with varied diameters of 50~100 nm. The obvious difference in morphology between CCFs and ACFs also indicates that the crystal growth of CCFs could be regulated by coordination interactions between His and Cu ions during the

formation process.

The TEM image (Fig. 1c$_1$) shows that the sample is consist of several fusiform nanoparticles with rough surfaces. The high-magnification TEM image (Fig. 1c$_2$) shows that each Cu nanoparticle is composed of a single crystalline core (indicated by the white dashed line) surrounded by polycrystalline Cu nanocrystals (Fig. S5). The Fourier diffractogram (FD) indicates the strong sharp reflection corresponding to the 111 lattice plane of the core and the ring pattern generated by the edge polycrystals (Fig. S5).

However, the polycrystalline nature of this material makes it very difficult to determine the exposed kink sites. Herein, the high-angle annular dark-field scanning transmission electron microscopy (HAADF-STEM) has been employed, which relies on the mass-thickness contrast and is highly sensitive to the atomic numbers. As shown in Fig. 1d, each white dot corresponds to a high electron-scattering density, i.e., a column of Cu atoms. For thin crystals, it can be expected that the observed intensity (brightness) of the column of atoms is linearly correlated to the atomic number. Although the distortion of the atomic layers is realized in the Figure, the fourfold symmetry can still be recognized from most part of the particle, suggesting the [001] axis. Therefore, to semi-quantitatively determine the crystal structure, we combined the 2D projection of the image and the intensity distribution for each column of atoms extracted using software Gatan DigitalMicrograph (Fig. S6). The atom number for each column was determined from the peak intensity according to their largest common divisor by removing the common background, which clearly reveals the equi-multiple relationship corresponding to the number of Cu atoms (Table S1). The numbers on the atoms in Fig. 1e$_1$ show the possible number of Cu atoms in the column along the z direction. Accordingly, a structural model was established based on the atomic number and the basic principle of close packing that the atoms are located on the nearest tetrahedron sites while keeping the smallest packing volume.

As shown in Fig. 1e$_{2-4}$, not only conventional crystal faces of the FCC lattice (111, 110 and 100) but also chiral kink sites (653)^S can be identified in the model (Fig. 1e$_5$), suggesting the possible existence of chiral kink sites on Cu surfaces. Because polycrystalline nanobuds are randomly distributed on the surface of the nanoparticle, several high-index facets are expected (Fig. S7). Although other chiral kink sites reported previously[28,29] are not identified in the current structural model, we also considered their possible formation induced by His *via* density functional theory (DFT) calculations.
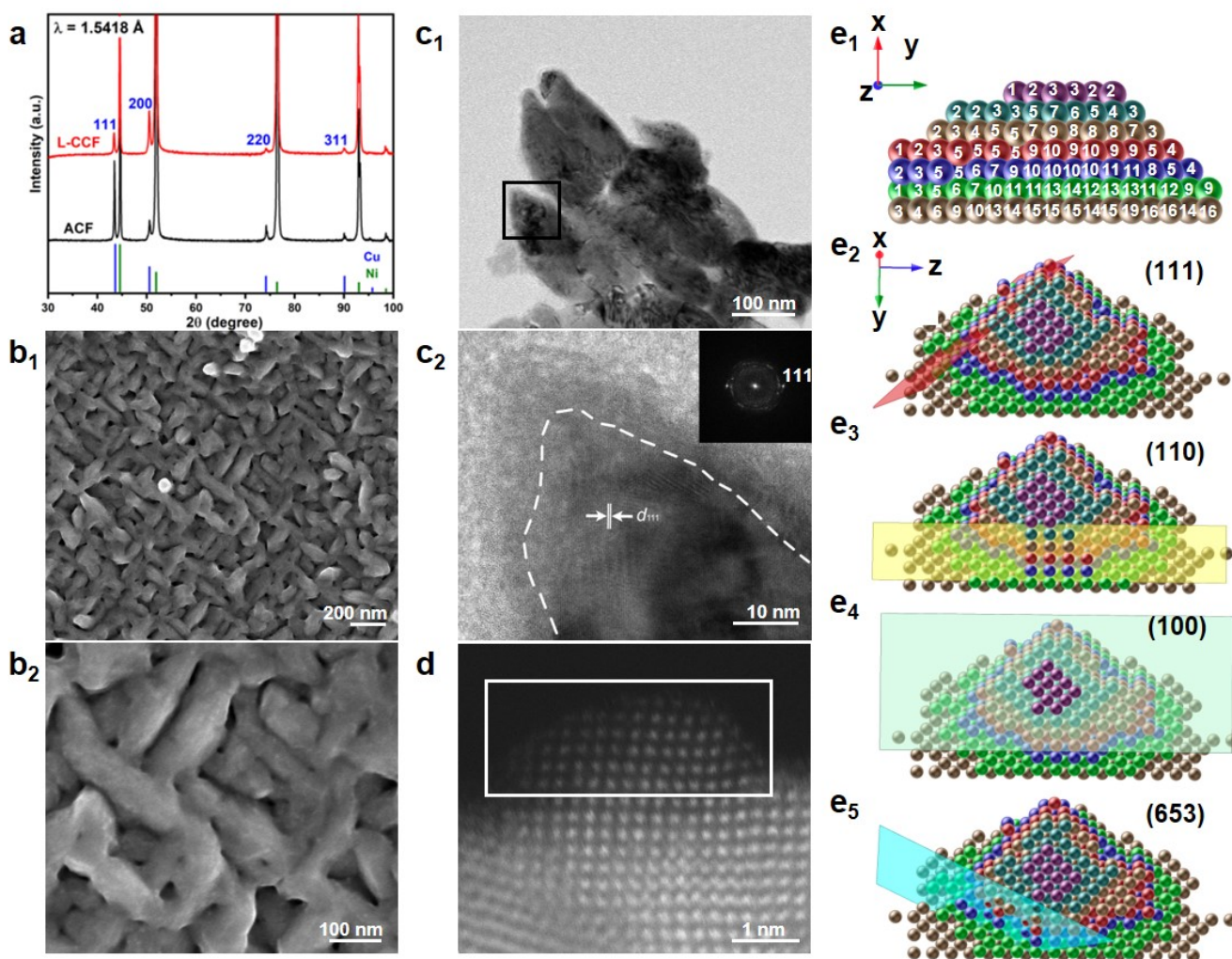

Fig. 1 | Morphologies and structures of L-CCFs. a, XRD patterns of the L-CCFs (red) and ACFs (black). The reflections of Ni and Cu are marked by blue and green bars, respectively. **b,** Low- (b$_1$) and high-magnification (b$_2$) SEM images of L-CCFs. **c,** Low- (c$_1$) and high-magnification (c$_2$) TEM images of L-CCFs. **d,** HAADF-STEM image of L-CCFs, **e$_1$,** Schematic drawing of the structural model with the number of atoms in the corresponding column of Cu atoms. **e$_{2-5}$,** Slab surface models of (111), (110), (100) and (653) obtained from the structural model reconstructed from the STEM image of L-CCFs. The synthetic molar composition was as follows: 1 CTAC:1.45 L-His: 0.8 K$_2$CuCl$_4$: 0.2 NiCl$_2$: 5208 H$_2$O : 224.8 KCl : 0.093 HCl. The applied electrochemical deposition potential was -1.1 V vs Hg/Hg$_2$SO$_4$ (saturated K$_2$SO$_4$).

To verify the structural model, the HAADF-STEM image was simulated based on the above model using software Elbis[30,31]. The simulation shows high similarity to our experimental image. Besides, the correlation between the number of the Cu atoms in the column and the intensity extracted from the image is shown in Fig. S8. Though there are slight deviations of the intensity distribution away from the ideal linear relationship, the intensity is basically proportional to the number of Cu atoms even the atom number reaches up to 19. These results strongly support our semi-quantitatively determination of the structural model and indicate that His can alter the crystal growth of Cu to increase the number of repeating units along the <100> axis. The distortion of the crystal structure observed in the STEM image, which may be generated by the slicing process for sample preparation towards TEM observation.

On the other hand, the TEM image of ACFs shows the single crystalline feature of the Cu nanoparticle (Fig. S9). Judging from the corresponding crystal morphology and the ED pattern, all exposed crystal faces can be assigned to low-index lattice planes, from which {111} was mostly observed. This finding is consistent with the FCC structure in which {111} has the largest packing density.

The chiral kink sites on CCF surfaces should endow the Cu atomic arrays with optical activity due to the chirality of electron cloud induced by the shift of Cu atoms on the CCF surfaces in the asymmetric configuration, which can be detected via diffused reflection circular dichroism (DRCD)[32]. DRCD spectra (Fig. S10a) of the antipodal CCFs show mirror-image CD signals at 300~600 nm corresponding to the Cu surface plasmon resonance peak in the UV-Vis absorption spectrum[33]. The transmission (T) CD spectra of antipodal His confirm again the absence of L-His on CCFs (Fig. S10b). The CD spectra of the ACFs showed no peak, indicating no chiral arrangement of Cu on the ACF surfaces was formed.

In addition to the experimental characterization above, we used DFT calculations to confirm the most likely chiral kink site induced by L-His from a number of possible chiral surfaces known to be present in Cu crystals[28,29] (Fig. S11a) to further confirming chiral atomic arrangement on CCFs surfaces. Fig. S11b shows the adsorption energies of L- and D-His on eight Cu chiral kink sites with S-chirality. The adsorption energies of L-His on $Cu(651)^S$, $Cu(653)^S$ and $Cu(17,5,1)^S$ are lower than those of other chiral Cu kink sites (Fig. S11b, Table S2). In addition, L-His adorption energies on $Cu(651)^S$ and $Cu(653)^S$ are lower than its D-His adsorption energies indicating the formation of these three chiral kink sites on the L-CCF surfaces would be possibly induced via L-His adsorption. However, considering L- and D-his induced formation of the L- and D-CCFs antipodal surfaces, respectively. According to DFT calculations, $Cu(651)^S$ and $Cu(653)^S$ are most possible to be induced via L-His adsorption on the L-CCFs, and vise cersa via D-His.
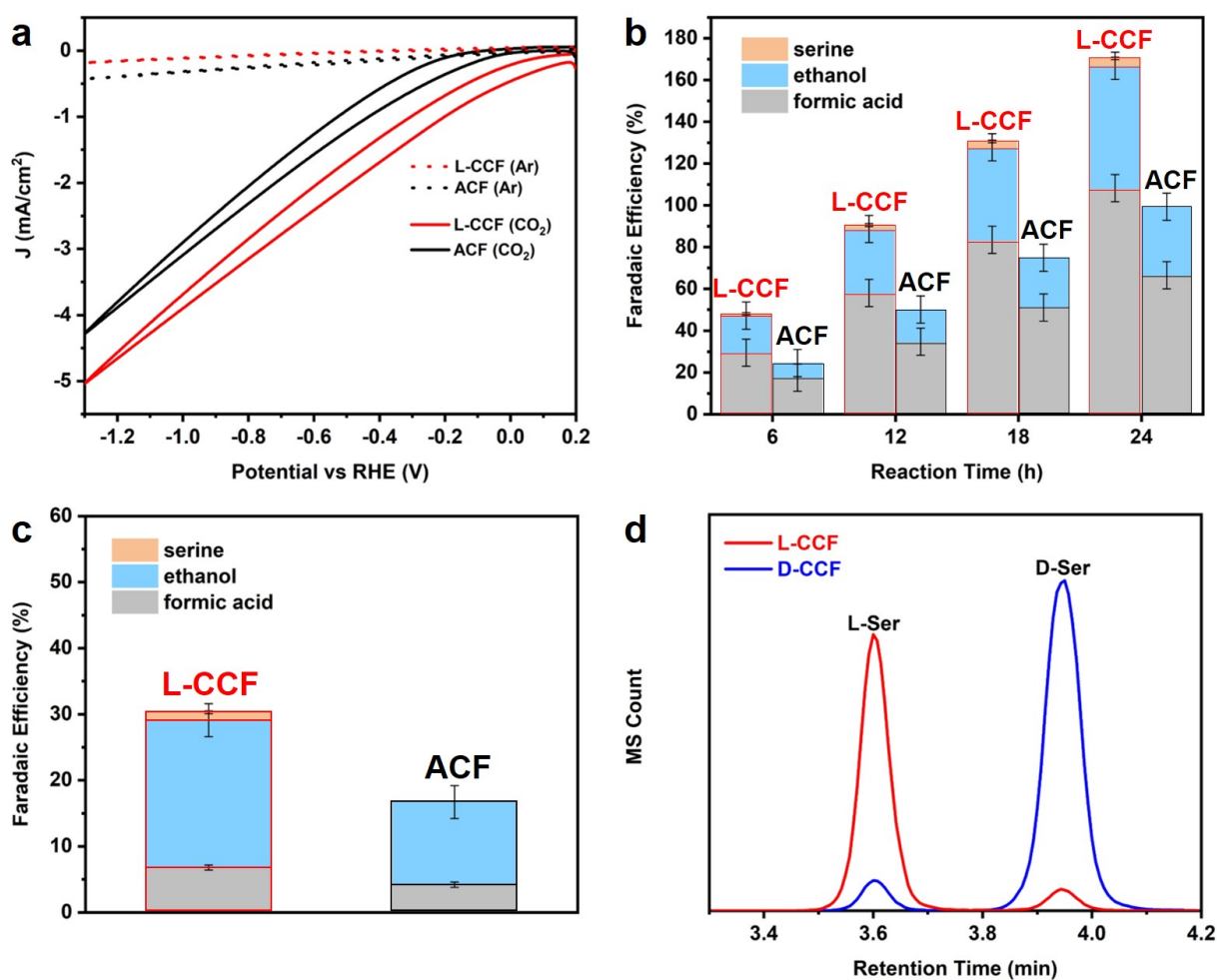

Fig. 2 | Enantioselective formation of Ser on CCFs. a, Current density of L-CCFs and ACFs in 0.25 M $NH_3 \cdot H_2O$ under 4.5 MPa Ar and 0.25 M NH_4HCO_3 under 4.5 MPa CO_2, respectively. **b,** Time-dependent formation of Ser, ethanol and formic acid in the L-CCF and ACF catalytic systems (the volume of electrolyte is 60 ml). **c,** FEs of Ser, ethanol and formic acid in the L-CCF and ACF catalytic systems. **d,** HPLC-MS of Ser obtained with L- and D-CCFs in 0.25 M NH_4HCO_3 under 4.5 MPa CO_2 at a CV potential between -0.5 V and -1.3 V vs. RHE for 24 h.

Formation of enantiomeric excess amino acids by electrocatalytic reduction of CO_2 with CCFs

To synthesize amino acids by electrocatalytic reduction of CO_2, an NH_4HCO_3 aqueous solution was selected as both the electrolyte and nitrogen source. CO_2 electrocatalytic reduction was carried out in a three-electrode H-pressure cell using L-CCF, D-CCF and ACF catalysts as working electrodes.

Fig. 2a shows the cyclic voltammetry (CV) curves of CO_2 reduction using L-CCFs and ACFs as working electrodes under 4.5 MPa of CO_2, which exhibit reduction peaks in the range of 0.2 to -1.3 V and a higher reduction current of L-CCFs than of ACFs. The reduction current of both films under 4.5 MPa of Ar is ~5 % of that under 4.5 MPa of CO_2. The average geometric current density of CO_2 reduction in the L-CCF and ACF systems was calculated to be 3.17 and 2.46 mA/cm^2, respectively, indicating that CO_2 reduction occurs at potentials between -0.3 and -1.3 V, and the catalytic activity of the L-CCFs was greater than that of the ACFs.

To quantitatively analyze CO_2 reduction intermediates and products, *in situ* photoionization mass spectrometry (PIMS) was employed. As shown in Fig. 2b and Fig. S12, when using L-CCFs as the working electrode, Ser, ethanol and formic acid were formed, and their formation increased with time, resulting in ~3.8 (±0.6), ~58.6 (±6.5) and ~108.1 (±6.5) μmol after 24 h CV, respectively. Compared to L-CCFs, no Ser was formed using ACFs as working electrodes, and the yields of ethanol and formic acid (~32.8 (±6.5) and ~66.4 (±6.5) μmol) were much lower than those in the L-CCF reaction system. Interestingly, 3-hydroxypyruvic acids were observed intermittently when using CCFs as catalysts, while 3-hydroxypyruvic acid was scarcely observed when using ACFs as catalysts (Fig. S12c).

Fig. 2c shows that the Faradaic efficiencies (FEs) of Ser, ethanol and formic acid were ~1.2 (±0.2), ~22.3 (±2.5) and ~6.8 (±0.4) %, respectively, in the L-CCF reduction system. When using an ACF as the working electrode, the FEs of ethanol and formic acid were ~12.5 (±2.5) and ~4.2 (±0.4) %, respectively, indicating that the chiral kink sites of the L-CCF surface enhanced the CO_2 reduction catalytic activity, especially for the C_2 and C_3 products. Fourteen kinds of amino acids were formed in the L-CCF catalytic system (Table S3), and the molar amount of Ser was 30~100 times higher than that of other amino acids when using CV method for CO_2 reduction. However, when applying electrocatalysis at a constant potential, the yield of Ser was severely decreased (Table S3), which might be because the adsorption states of the reagents remained steady, similar to the situation in a previous report[18]. This means that the interference of the 111 lattice surfaces of L-CCFs could be suppressed by using the CV method for CO_2 electroreduction.

The *ee* value of Ser produced with achiral CCFs was determined by high-performance liquid chromatography-mass spectrometry (HPLC-MS) after derivatization by *N*-(5-fluoro-2,4-dinitrophenyl)-L-leucinamide. As illustrated in Fig. 2d, different proportions of L- and D-Ser were observed at retention times of 3.60 and 3.94 min, respectively. In the L- and D-CCF electrocatalyst systems, Ser with *ee* values of 94.0 (±0.5) and -91.2 (±0.5) % was obtained, respectively.

Control experiments using L-His-adsorbed ACFs (ACFs-L-His) as a catalyst were carried out to exclude the effect of L-His on the catalytic activity for the formation of Ser. An L-His aqueous solution was dropped onto ACFs and dried at room temperature for 12 h. The presence of L-His on ACF films was confirmed by N 1s XPS (Fig. S13) and the amount of L-His adsorbed on ACFs-L-His was estimated to be ~67 μg/cm^2 from the loaded amount of L-His and geometric area of ACFs. The products generated by ACFs-L-His were almost the same as those generated by ACFs, indicating that the chiral kink sites play a key role in catalysis rather than L-His (Table S3).
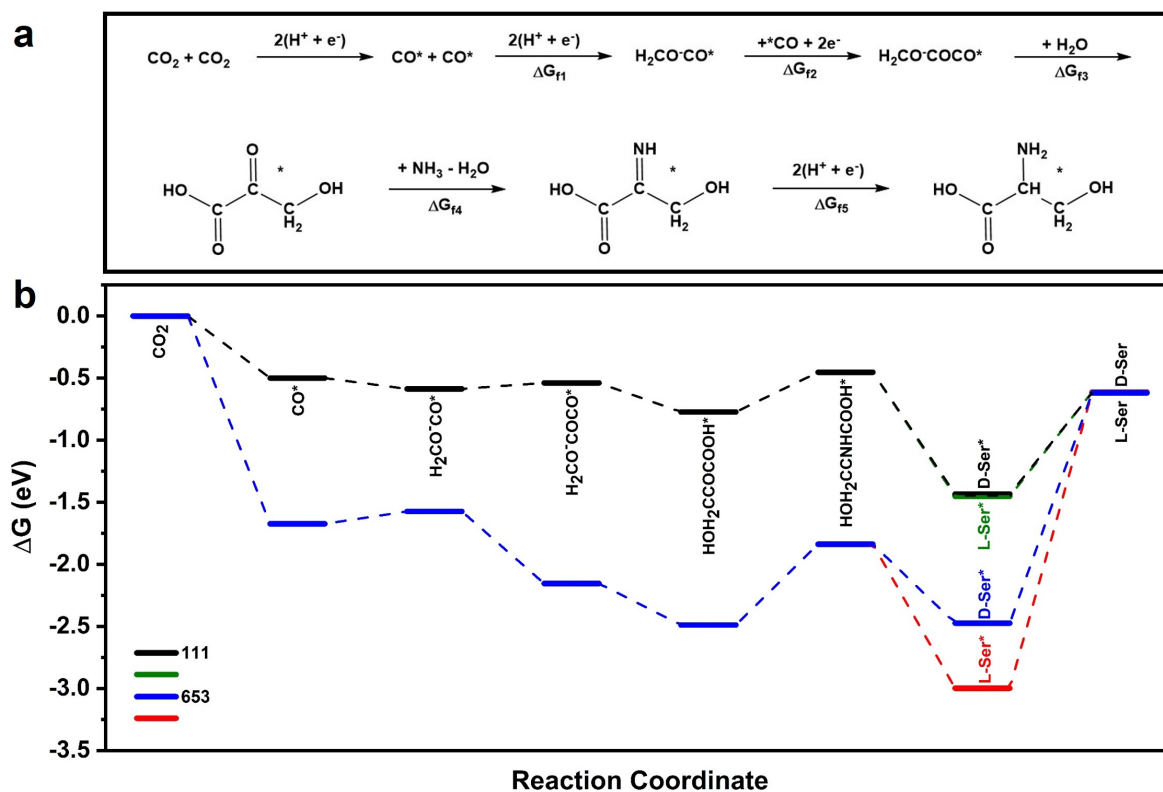

Fig. 3 | DFT calculations for the enantioselective formation of Ser. a, Overview of the Ser formation pathway from CO_2 and NH_3 *via* electroreduction. **b,** adjusted Gibbs free energy profile corrected by the pressure of 4.5MPa, of the intermediates for the formation of antipodal Ser on Cu(111) and Cu(653). In addition, Gibbs free energy profile corrected by the pressure of 1 atm ($\approx$0.101325 MPa) is in Fig. S14 for estimation on thermodynamic preference of catalysis at standard atmospheric pressure.
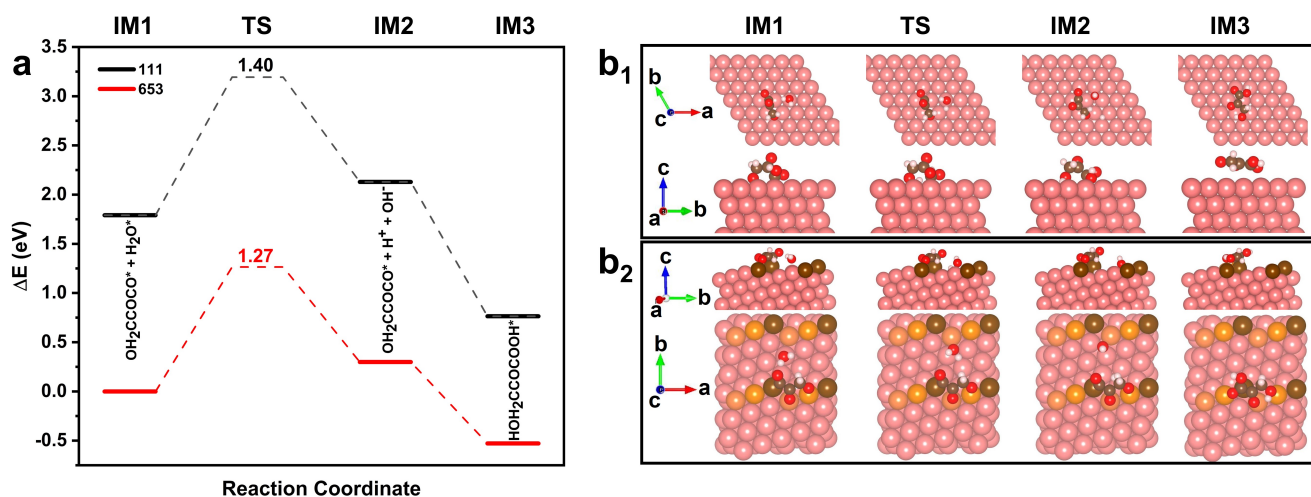
Fig. 4 | DFT calculations for kinetics energy profiles about the transition states in the formation of 3-hydropyruvic acid, which is the stereoselective intermediates. a, energy profiles of formation of 3-hydropyruvic acid on (111) and (653); **b,** corresponding atomic models of transition states and intermediates in energy profiles on (111) (b₁) and (653) (b₂).

CO₂ reduction pathway for Ser

Fig. 3a shows our proposed pathway for Ser formation based on the mechanism of CO_2 reduction for ethanol[3,11] and pyruvic acid[34,35] and electrosynthesis for amino acids[36], as suggested in the literatures. This pathway is consistent with the PIMS data for CO_2 reduction, where H_2CO^-COCO* is generated through the coupling reaction of OH_2CCO* with $CO*$; 3-hydropyruvic acid is then generated from hydrolysis of H_2CO^-COCO*; and finally, Ser is synthesized *via* amination with ammonia to form 3-hydropyruvic acid.

DFT simulation for the formation of Ser from CO₂ reduction

To understand the formation of antipodal Ser with high *ee* values from CO_2 and NH_3 on antipodal chiral surfaces, we employed DFT calculations to evaluate the enantioselective formation pathway of Ser on different Cu surfaces. Cu(653)^S was estimated to be most active sites and chosen as the model of chiral surfaces due to its largest energy preference in adsorbing different Ser enantiomers (Fig. S15).

Fig. 3b shows the Gibbs free energy profiles for the intermediates of CO_2 reduction on Cu(653)^S and Cu(111) (Table S4). Obviously, the reaction on Cu(653)^S is thermodynamically favorable due to the preferable adsorption of all intermediates. In particular, the Gibbs free energy of H_2CO^-COCO* formation from H_2CO^-CO* on Cu(653)^S is -0.58 eV, which is 0.61 eV lower than that of Cu(111). Since $H_2COCOCO*$ is an essential intermediate for formation of 3-hydropyruvic acid, the results rationalize the formation of 3-hydropyruvic acid on L-CCFs but almost none on ACFs. The higher adsorption energy of 3-hydroxypyruvic acid can be attributed to the simultaneous interaction of carbonyl, hydroxyl and carboxyl groups with the surface Cu atoms at the kink edge of Cu(653)^S (Fig. S16). Our experiments also show that 3-hydroxypyruvic acid was formed intermittently on L-CCFs but was not detected on ACFs. From DFT energetics and experimental evidence, we conclude that 3-hydroxypyruvic acid is the key intermediate in Ser formation, which can be strongly stabilized by L-CCF catalysts.

DFT simulation of the enantioselectivity for Ser of chiral kink sites

Fig. 3b also compares the Gibbs free energy for the formation of antipodal Ser on Cu(653)^S and Cu(111) (Table S5). On Cu(653)^S, the Gibbs free energy for L-Ser formation is lower than that for D-Ser formation by 0.524 eV, which accounts for the observed enantioselectivity in Ser formation on CCF catalysts. This is due to the preferable adsorption of L-Ser due to the orientation of its hydroxymethyl and carboxyl group structurally compatible with Cu(653)^S kink edges (Fig. S16). On

the other hand, the difference in Gibbs free energies for the formation of L-Ser and D-Ser on Cu(111) is only 0.018 eV. These theoretical results are in line with the distinct differential pulse voltammetry (DPV) for the electrooxidation of L-Ser and D-Ser on L-CCFs and D-CCFs (Fig. S17).

DFT simulation of the transition states (TS) in the formation of 3-hyropyruvic acid

Fig. 4 shows the reaction profile for the key kinetics step in 3-hyropyruvic acid formation, i.e. H_2CO^-COCO to $HOH_2CCOCOH$, on Cu(111) and Cu(653)^S. In this stereoselective step, we found that the TS is 0.13 eV in energy on (653) lower than it on Cu(111), which is obviously due to the lower coordination Cu atoms on Cu(653). This confirms that 3-hyrdopyruvic acid is also kinetically preferable on Cu(653) and energy barriers in serine formation on these Cu surfaces are mainly occurred from a kinetic hindrance. We note that at the TS on Cu(653) surface can provide two Cu atoms, which possess the coordination number of 8 and 9 to stabilize the dissociating H---OH, respectively, while Cu(111) surface has only one Cu atom with the coordination number of 9 involved in reaction. Consistently, the reacting H---O distance at the TS on (653) (1.454 Å) is 0.250 Å shorter than that on Cu(111). As shown in Fig. 4b and Fig. S18, the structural configuration undergoes a large change in the reaction on Cu(111) compared to it on Cu(653), suggesting the extra rotation and translation are needed in producing the product from the initial reactant and thus the activation energy on Cu(111) is higher. The Cu(653) provides a uniform structure template to stabilize H_2CO^-COCO* and the subsequent intermediates.

Conclusions

To the best of our knowledge, the electrocatalytic reduction of CO_2 into enantiomeric amino acids is the first example of complex C_{3+} products with C-N bonds of CO_2 electrocatalytic reduction. The chiral kink sites were discovered to confine the configuration of C_{3+} intermediates on catalysts surfaces, leading to the decrease of reaction barriers in synthesis of C_{3+} products from CO_2 reduction. Although the major amino acids product is Ser, various amino acids and urea were observed as products as well. Thus, there is the potential application of chiral kink sites for obtaining desire biomolecules starting with CO_2 and ammonium bicarbonate. Moreover, inducing chiral kink sites into catalytic system would be a universal approach for improving intrinsic activities of catalytic materials for synthesis of C_{3+} species.

References

1 Classens, N. J. et al. Harnessing the power of microbial autotrophy. *Nat. Rev. Microbiol.* **14,** 692-706 (2016).

2 Grim, R. G. et al. Transforming the carbon economy: challenges and opportunities in the convergence of low-cost electricity and reductive CO_2 utilization. *Energy Environ. Sci.* **13**, 472-494 (2020).

3 Nitopi, S. et al. Progress and perspectives of electrochemical CO_2 reduction on copper in aqueous electrolyte. *Chem. Rev.* **119**, 7610-7672 (2019).

4 Hahn, C. et al. Engineering Cu surfaces for the electrocatalytic conversion of CO_2: Controlling selectivity toward oxygenates and hydrocarbons. *Proc. Natl. Acad. Sci. U.S.A* **114**, 5918-5923 (2017).

5 Liu, X. et al. pH effects on the electrochemical reduction of $CO_{(2)}$ towards C_2 products on stepped copper. *Nat. Commun.* **10**, 32 (2019).

6 Liang, Z. et al. Copper-on-nitride enhances the stable electrosynthesis of multi-carbon products from CO_2. *Nat. Commun.* **9**, 3828 (2018).

7 Xie, H. et al. Cu-based nanocatalysts for electrochemical reduction of CO_2. *Nano. Today.* **21**, 41-54 (2018).

8 Li, Q. et al. Controlled assembly of Cu nanoparticles on pyridinic-N rich graphene for electrochemical reduction of CO_2 to ethylene. *Nano Energy* **24**, 1-9 (2016).

9 Vasileff, A. et al. Surface and interface engineering in copper-based bimetallic materials for selective CO_2 electroreduction. *Chem* **4**, 1809-1831 (2018).

10 Chen, L. et al. Spatial-confinement induced electroreduction of CO and CO_2 to diols on densely-arrayed Cu nanopyramids. *Chem. Sci.* **12**, 8079-8087 (2021).

11 Handoko, A. et al. Understanding heterogeneous electrocatalytic carbon dioxide reduction through operando techniques. *Nat. Catal.* **1**, 922-934 (2018).

12 Kuhl, K. et al. New insights into the electrochemical reduction of carbon dioxide on metallic copper surfaces. *Energy Environ. Sci.* **5**, 7050-7059 (2012).

13 Tao, Z. et al. Cascade electrocatalytic reduction of carbon dioxide and nitrate to ethylamine. *J. Energy Chem.* **65**, 367-370 (2022).

14 Chen, C. et al. Coupling N_2 and CO_2 in H_2O to synthesize urea under ambient conditions. *Nat. Chem.* **12**, 717-724 (2020).

15 Jouny, M. et al. Formation of carbon–nitrogen bonds in carbon monoxide electrolysis. *Nat. Chem.* **11**, 846-851 (2019).

16 Wu, Y. et al. Direct electrosynthesis of methylamine from carbon dioxide and nitrate. *Nat. Sustain.* https://doi.org/10.1038/s41893-021-00705-7 (2021).

17 Zhuang, T. et al. Steering post-C–C coupling selectivity enables high efficiency electroreduction of carbon dioxide to multi-carbon alcohols. *Nat. Catal.* **1**, 421-428 (2018).

18 Lum, Y. & Ager, J. W. Evidence for product specific sites on oxide-derived Cu catalysts for electrochemical CO_2 reduction. *Nat. Catal.* **2**, 86-93 (2019).

19 Cheng, D. et al. The nature of active sites for carbon dioxide electroreduction over oxide-derived copper catalysts. *Nat. Commun.* **12**, 395 (2021).

20 McFadden, C, F. et al. Adsorption of Chiral Alcohols on "Chiral" Metal Surfaces. *Langmuir* **12**, 2483-2487 (1996).

21 Gellman, A, J. et al. Structure-sensitive enantiospecific adsorption on naturally chiral Cu(hkl)[R&S] surfaces. *J. Phys.: Condens. Matter.* **29**, 034001-034011 (2017).

22 Lopez, N. et al. On the origin of the catalytic activity of gold nanoparticles for low-temperature CO oxidation. J. Catal. **223**, 232-235 (2004).

23 Hazen, R. M. & Sholl, D. S. Chiral selection on inorganic crystalline surfaces. *Nat. Mater.* **2**, 367-374 (2003).

24 Harazzi, O. A. et al. Molecular recognition in adsorption and electro-oxidation at chiral platinum surfaces. *J. Mol. Catal. A-Chem.* **216,** 247-255 (2004).

25 Wattanakit, C. et al. Enantioselective recognition at mesoporous chiral metal surfaces. *Nat. Commun.* **5**, 3325 (2014).

26 Yutthalekha, T. et al. Asymmetric synthesis using chiral-encoded metal. *Nat. Commun.* **7**, 12678 (2016).

27 Grousier, J. & Bimaghra, I. Effect of nickel on the electrodeposition of copper. *J. Appl. Electrochem.* **23**, 775-780 (1993).

28 Gellman, A, J. et al. Structure-sensitive enantiospecific adsorption on naturally chiral Cu(hkl)[R&S] surfaces. *J. Phys.: Condens. Matter.* **29**, 034001-034011 (2017).

29 Yun, Y. & Gellman, A, J. Enantioselective separation on naturally chiral metal surfaces: D,L-aspartic acid on Cu(3,1,17)[R&S] surfaces. *Angew. Chem. Int. Ed.* **52**, 3394-3397 (2013).

30 Hosokawa, M. et al. Benchmark test of accelerated multi-slice simulation by GPGPU. *Ultramicroscopy* **158**, 56-64 (2015).

31 Hosokawa, M. et al. Image transfer with spatial coherence for aberration corrected transmission electron microscopes. *Ultramicroscopy* **167**, 11-20 (2016)

32 Ma, W. et al. Chiral inorganic nanostructures. *Chem. Rev.* **117**, 8041-8093 (2017)

33 Wang, Y. et al. Synthesis of well-defined copper nanocubes by a one-pot solution process. *Nanotechnology* **17**, 6000-6006 (2006).

34 Rodan, A. et al. Bio-inspired CO_2 conversion by iron sulfide catalysts under sustainable conditions. *Chem. Commun.* **51**, 7501-7504 (2015).

35 Varma, S. J. *et al.* Native iron reduces CO_2 to intermediates and end-products of the acetyl-CoA pathway. *Nat. Ecol. Evol.* 2, 1019-1024 (2018).

36 Fukushima, T. & Yamauchi, M. Electrosynthesis of amino acids from biomass-derivable acids on titanium dioxide. *Chem. Commun.* **55**, 14721-14724 (2019).

37 Valtz, A. *et al.* Vapour–liquid equilibria in the carbon dioxide–water system, measurement and modelling from 278.2 to 318.2 K. *Fluid Phase Equilibria* **226**, 333-344 (2004).

Supplementary Information is available in the online version of the paper.

Author Contributions

Y. F. conceived the idea and S. C. led the project. Y. F. synthesized the materials, performed the SEM, CD, XRD, electrochemical measurements and HPLC enantiomer measurements; L. H., O. T., X. L., J. A., G. Z. and L. C. worked on the structural characterization through HRTEM; Z. L. and Y. F. contributed to the theoretical calculations; J. Y., G. Z., C. C., C. L. and Z. Z. contributed to PIMS analysis; Y. F., S. C., L. H. and Z. L. contributed to the analysis of mechanism and the preparation of manuscript.

METHODS：

Synthesis of CCFs

In a typical synthesis, 0.026 g of CTAC and 1.18 g of KCl were dissolved in 4.5 ml distilled water, and then 1 ml 120 mM L-His (chirality-inducing agent), 0.8 ml of 80 mM potassium tetrachlorocuprate in 3 M KCl, 0.2 ml of 80 mM nickel chloride in 3 M KCl and 7.6 μL of 1 M HCl were added to the solution successively. Then, the solution was stirred over 3 h to stabilize the self-assembly in solution. Cu was deposited at a constant potential of -1.1 V *vs* Hg/Hg_2SO_4 for 3000 s using a CHI760E equipped with a mercurous sulfate electrode (saturated potassium sulfate) as the reference electrode, a Pt wire as the counter electrode, and Ni foil as the working electrode. Subsequently, the deposited film was washed with water, soaked in ethanol and subjected to 50 cycles of CV in 0.1 M $HClO_4$ from -0.375 V to -0.05 V *vs* Ag/AgCl to remove the organic molecules (CTAC and L-His). After cleaning, CCFs were vacuum dried at room temperature for preservation.

Electroconversion from CO_2 to enantiomeric excessed amino acids

Electrochemical synthesis of enantiomeric excess amino acids on CCFs was performed *via* CV from -1.1 V to -1.8 V for 24 h with a scan rate of 50 mV/s in an aqueous solution of 0.25 M NH_4HCO_3 as the supporting electrolyte and addition of the CO_2 into an H-pressure cell (Gaoss Union, P003-2) separated by an anion exchange membrane (Membranes International Inc., AMI-7001) to a pressure of 4.5 MPa. All experiments were carried out using a CHI760E equipped with Ag/AgCl (saturated NaCl), a Ti/RuO_2-IrO_2 plate and the CCFs as the reference, counter and working electrodes, respectively. The pH of the CO_2-saturated 0.25 M ammonium bicarbonate solution under 4.5 MPa pressure was calculated to be 4.64 and the pH of 0.25 M ammonia is 11.32. The saturation concentration of CO_2 was calculated according to a previous report[37]. Electrode potentials were converted to RHE using the following equation. $E_{RHE} = E_{Ag/AgCl} + 0.197$ V $+ 0.0591 \times$ pH. The average geometric current of CO_2 reduction was calculated using the following equation: $E_{ave} = E_{ave(CO2)} - E_{ave(Ar)}$.

Finally, the solution was lyophilized to remove water. Then, the product was further purified by annealing at 80 °C overnight. The purified product was derivatized by L-FDLA before separation by HPLC-MS. To derivatize amino acid compounds, 10 mg of product was dissolved in 500 μL of DI water, and then 50 μL of an aqueous solution was mixed with 20 μL of 200 mM sodium bicarbonate and 20 μL of 1 % L-FDLA in acetone. The mixture was incubated at 37 °C for 30 min. After returning to room temperature, 200 μL of methanol was added to the sample, and the impurity was centrifuged (12000 rpm, 10 min). The sample was kept in the dark condition.

HPLC-MS analysis was performed by using an Acquity UPLC & XEVO G2-XS QTOF (Waters, United States) equipped with a UPLC column (Acquity UPLC HSS T3 1.8 μm, 2.1*100 mm). The detection of samples was conducted in positive ESI mode, and the function type was TOF-MS with a mass range of 200–600. Then, a 0.1 μL sample was injected and

eluted using mobile phase A (0.1% mass concentration of formic acid aqueous solution) and mobile phase B (acetonitrile) at a flow rate of 0.35 ml/min. The programmed mobile phase gradient was as follows: 0.00–1.00 min, 25% B; 1.00–4.30 min 35% B; 4.30–6.50 min 100% B; 6.50–40 min 25% B. The column was equilibrated prior to sample injection, and the temperature of the column oven was set at 45 °C.

To generate a standard curve of L- and D-Ser, the standard compounds were diluted in water at concentrations adjusted to be relevant to tissue contents. After derivatization, 10 μL of the standard solution was separated and detected using the HPLC-MS system.

The enantiomeric excess (*ee*) was calculated based on the integrated peak areas of L- and D-Ser as indicated in equation 1.

$$ee = (\text{L-Ser} - \text{D-Ser})/(\text{L-Ser} + \text{D-Ser}) \quad (1)$$

where L-Ser and D-Ser represent the obtained peak areas of L-FDLA derivatized L-Ser and L-FDLA-derivatized D-Ser, respectively. The standard error of the mean of the %*ee* was calculated by means of equation 2.

$$\text{s.e.m.} = S/n \quad (2)$$

where S is the standard deviation and n is the number of experiments.

The Faradaic efficiency (FE) per surface area of products was calculated as FE $= mnF/Jt$, where m is the molar number of species in products; n is the number of electrons transferred for species formation; F is the Faraday`s constant, which is 96485 C/mol, J is the current density of electrosynthesis; and t is the time of reaction.
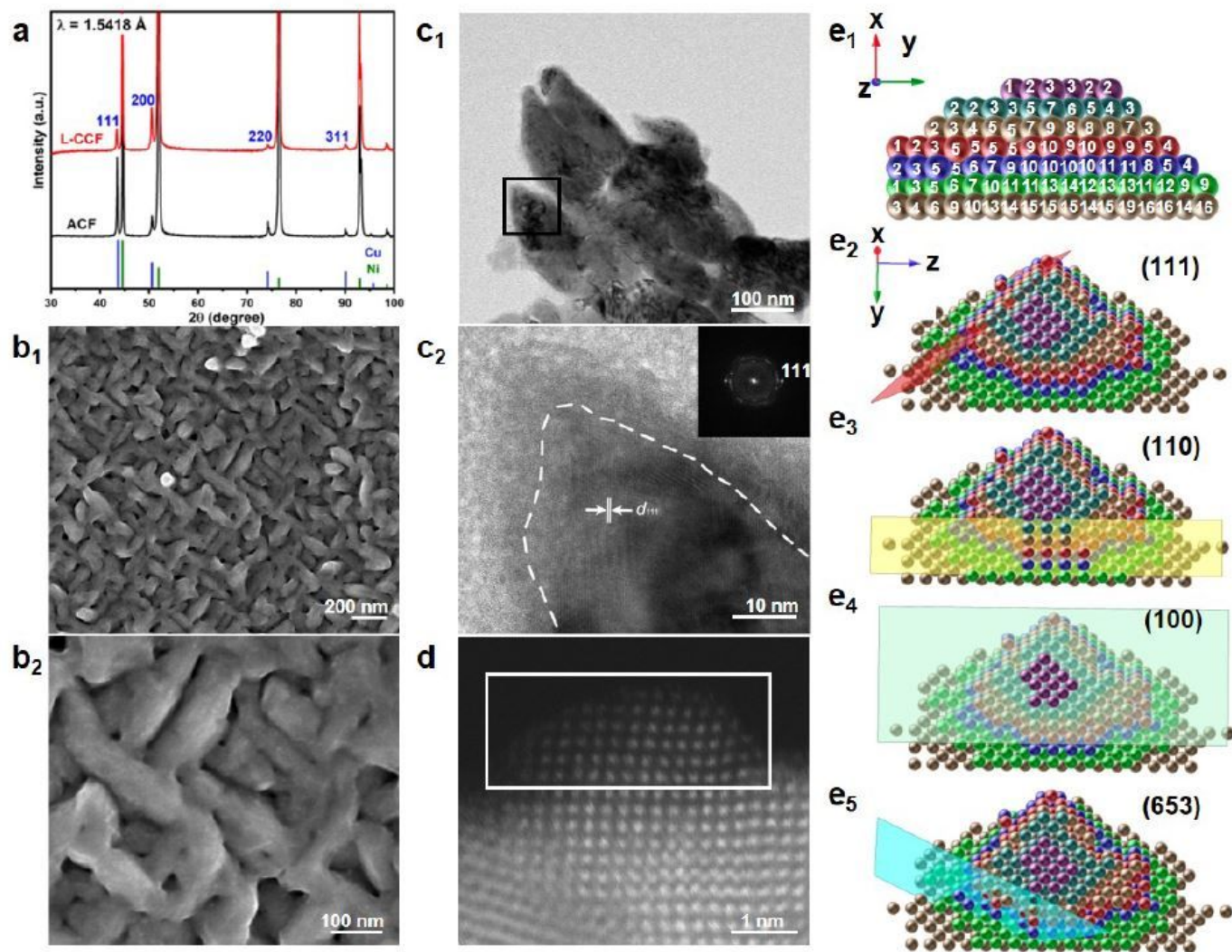
Figures

Figure 1

Morphologies and structures of L-CCFs. a, XRD patterns of the L-CCFs (red) and ACFs (black). The reflections of Ni and Cu are marked by blue and green bars, respectively. b, Low- (b1) and high-magnification (b2) SEM images of L-CCFs. c, Low- (c1) and high-magnification (c2) TEM images of L-CCFs. d, HAADF-STEM image of L-CCFs, e1, Schematic drawing of the structural model with the number of atoms in the corresponding column of Cu atoms. e2-5, Slab surface models of (111), (110), (100) and (653) obtained from the structural model reconstructed from the STEM image of L-CCFs. The synthetic molar composition was as follows: 1 CTAC:1.45 L-His: 0.8 K2CuCl4: 0.2 NiCl2 : 5208 H2O : 224.8 KCl : 0.093 HCl. The applied electrochemical deposition potential was -1.1 V vs Hg/Hg2SO4 (saturated K2SO4).
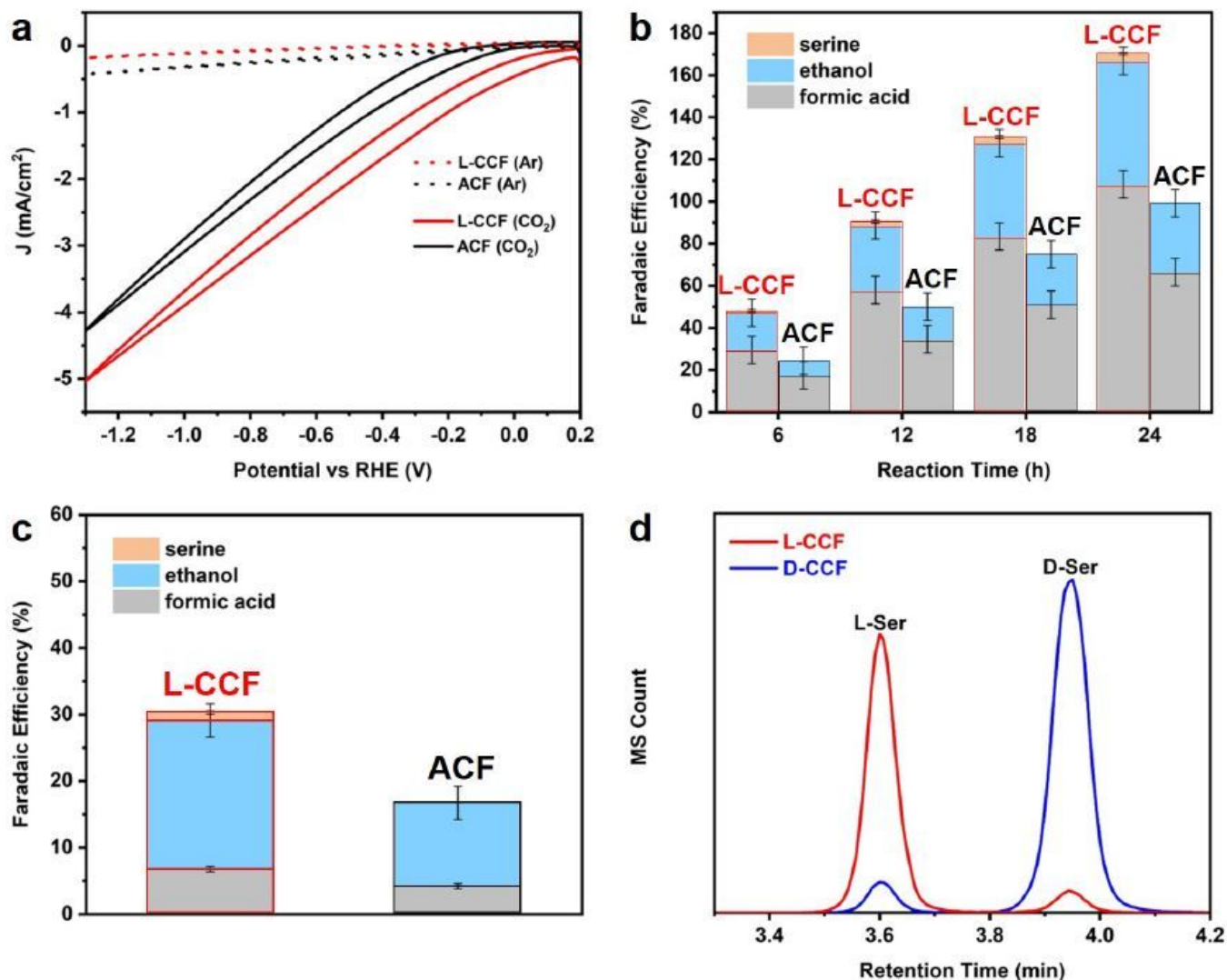
Figure 2

Enantioselective formation of Ser on CCFs. a, Current density of L-CCFs and ACFs in 0.25 M NH3·H2O under 4.5 MPa Ar and 0.25 M NH4HCO3 under 4.5 MPa CO2, respectively. b, Time-dependent formation of Ser, ethanol and formic acid in the L-CCF and ACF catalytic systems (the volume of electrolyte is 60 ml). c, FEs of Ser, ethanol and formic acid in the L-CCF and ACF catalytic systems. d, HPLC-MS of Ser obtained with L- and D-CCFs in 0.25 M NH4HCO3 under 4.5 MPa CO2 at a CV potential between -0.5 V and -1.3 V vs. RHE for 24 h.
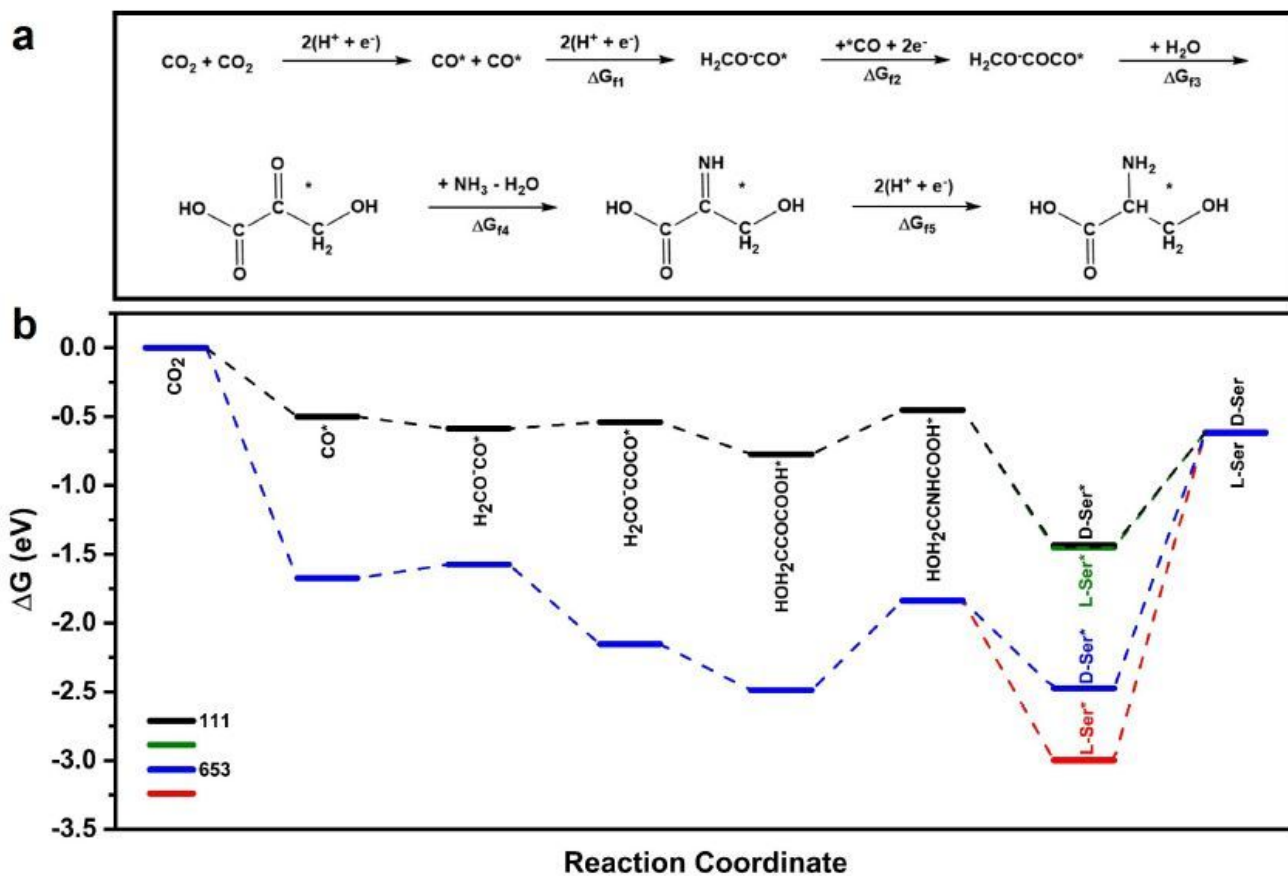
Figure 3

DFT calculations for the enantioselective formation of Ser. a, Overview of the Ser formation pathway from CO2 and NH3 via electroreduction. b, adjusted Gibbs free energy profile corrected by the pressure of 4.5MPa, of the intermediates for the formation of antipodal Ser on Cu(111) and Cu(653). In addition, Gibbs free energy profile corrected by the pressure of 1 atm (≈0.101325 MPa) is in Fig. S14 for estimation on thermodynamic preference of catalysis at standard atmospheric pressure.
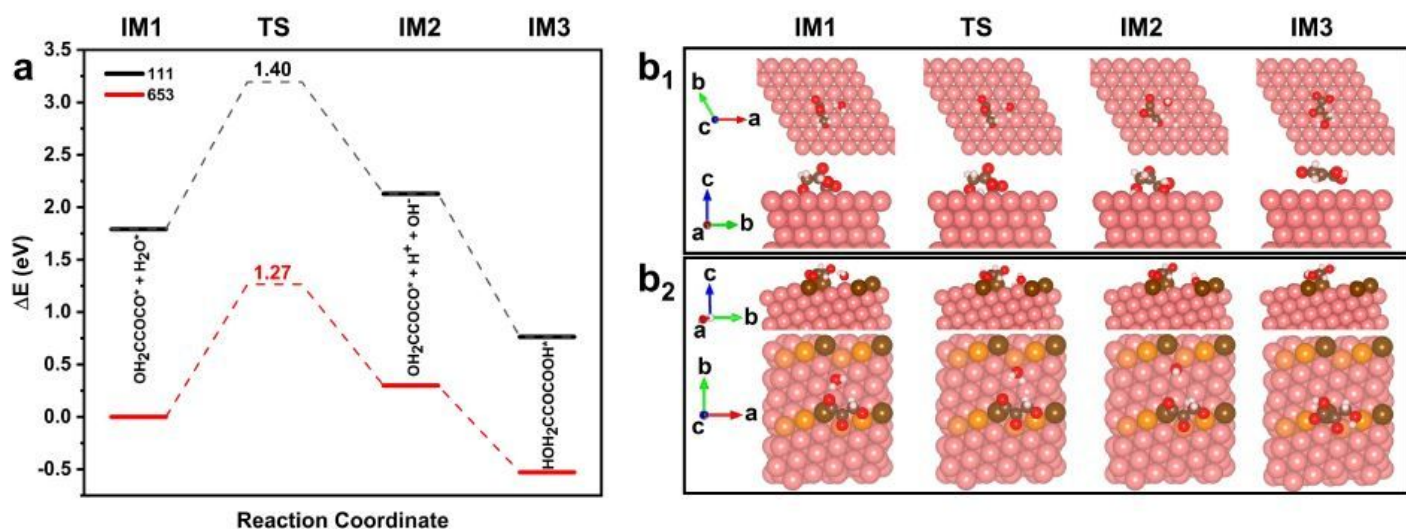
Figure 4

DFT calculations for kinetics energy profiles about the transition states in the formation of 3-hydropyruvic acid, which is the stereoselective intermediates. a, energy profiles of formation of 3-hydropyruvic acid on (111) and (653); b, corresponding atomic models of transition states and intermediates in energy profiles on (111) (b1) and (653) (b2).

Supplementary Files

This is a list of supplementary files associated with this preprint. Click to download.

- NCFYXSI.pdf
- NChemSIR1revised16488125983.pdf